Physics – Uspekhi **58** (9) 833 – 849 (2015)

REVIEWS OF TOPICAL PROBLEMS

PACS numbers: 61.05.C –, 61.72.Dd, 61.72.Ff

X-ray diffraction imaging of defects in topography (microscopy) studies

E V Suvorov, I A Smirnova

DOI: 10.3367/UFNe.0185.201509a.0897

Contents

Abstract. This review discusses how the X-ray diffraction images of crystal lattice defects form and acquire structure when using X-ray topography methods. Approaches for describing (ray optics and wave optics) and application fields of the geometrical and diffraction optics of a real crystal are analyzed. Specific experimental images of dislocations and other defects are used as examples to demonstrate the role of various diffraction effects (wave reflection from lattice distortions, diffraction focusing, channeling) in determining the character of the image formed. The potential for obtaining quantitative information on defect parameters is discussed.

Keywords: crystal structure defects, X-ray diffraction physics, X-ray topography, X-ray optics, diffraction contrast of defects, diffraction image, section topograms, Bloch waves, beam paths, elastic dislocation field, Takagi–Taupen equations, diffraction image simulation

1. Introduction

Modern physical materials science is inseparably related to the structural studies of substances (crystals, and solid solutions — alloys, amorphous systems, nanostructures, etc.), because it is their structural state that, often at the atomic level, determines essentially all their most important physical and service properties. Plasticity and hardness, strength, thermal, electric, and magnetic parameters, optical characteristics, etc., as a rule, are related to structural defects in crystals. Therefore, the problem of fabricating materials with prescribed properties is closely related to the improvement in existing materials and the development of new modern techniques for studying the real structure of materials. X-ray diffraction methods play a very important role in these studies. First, they give information on the internal structure of materials in a nondestructive manner and, second, these methods are, as a rule, quantitative and allow one to obtain the numerical values of the material structure parameters.

The idea of obtaining X-ray diffraction microscopic patterns (topograms) was first suggested by Berg [1] in 1931. This idea was further developed in numerous studies by Berg, Barrett, Fujiwara, Newkirk, Schulz, Kohra, Bonse, Borrmann, Lang, [2–10] and many others. For a long time, X-ray topography had only a qualitative, descriptive level and the X-ray images of crystal structure defects obtained by this method could not be used to retrieve any quantitative parameters of defects. Quantitative methods for the analysis of diffraction images were absent.

In 1959, A R Lang proposed a fundamentally new scheme for obtaining X-ray topograms (scan topograms, limited topograms, and section topograms) [11]. It is these schemes that initiated investigations into formation mechanisms of the X-ray diffraction images of crystal lattice defects. The scheme for obtaining topograms proposed by Lang is shown in Fig. 1.

The problem of X-ray imaging of defects was first discussed by Authier [12]. However, to understand the physics of X-ray imaging of defects in X-ray topography, the fundamentals were needed in the form of the dynamical theory of diffraction for crystals with their lattice distortions. The foundations of the X-ray scattering theory for perfect crystals developed by Darwin [13], Ewald [14], and Laue [15] back in the 1920s are reviewed in an excellent monograph by Cowley [16]. In our country, the first fundamental book on the classical dynamical theory of X-ray scattering in perfect

E V Suvorov, I A Smirnova Institute of Solid State Physics, Russian Academy of Sciences,
ul. Akademika Ossipyana 2, 142432 Chernogolovka, Moscow region, Russian Federation
E-mail: suvorov@issp.ac.ru, irina@issp.ac.ru

Received 5 May 2015
Uspekhi Fizicheskikh Nauk **185** (9) 897 – 915 (2015)
DOI: 10.3367/UFNr.0185.201509a.0897
Translated by M Sapozhnikov; edited by A Radzig

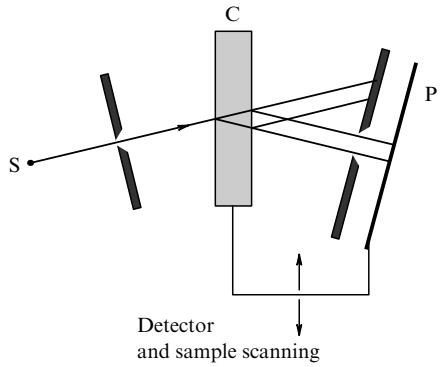

Figure 1. X-ray schematic of the Lang method: S is an X-ray point source, C is a single-crystal sample, and P is a detector (photographic plate) for topogram recording. The simultaneous displacement (scanning) of the sample and detector allows large areas of the crystal to be examined.

crystals was the translation of the monograph written by R W James and edited in Russian by V I Iveronova [17]. However, it is known that defects cause local distortions of a crystal lattice (local strains) and the description of radiation scattering by such distortions requires a more complex dynamic theory of X-ray scattering in *real crystals*.

Such theories have been developed already for more than 60 years. One of the first attempts in this area is probably the work by Takagi [18] in which the displacements of atoms caused by thermal vibrations are taken into account in the dynamic approximation.

Of great importance for understanding the mechanisms of X-ray scattering in real crystals were studies of diffraction in elastically bent crystals performed by Penning and Polder [19, 20]. However, this problem was investigated most fundamentally by N Kato in a series of papers [21–29] in 1962–1973, where he described for the first time the fundamentals of X-ray geometrical optics of crystals containing elastic strains.

The dynamic theory was generalized by Dederichs [30, 31] for crystals containing statistically distributed point defects. In the 1970s, M A Krivoglaz and researchers of his scientific school formulated the basic physical principles of X-ray scattering within the framework of the kinematic theory for crystals with statistically distributed point defects, and later on these principles were used as the basis for the dynamical theory of radiation scattering in real crystals [32, 33].

At about the same time (1962–1965), S Takagi in Japan and D Taupen in France proposed a more general approach to the problem of X-rays scattering by weak distortions of the crystal lattice. As a result, they arrived at a rather universal system of differential equations (called Takagi–Taupen equations) describing this complex process in the two-wave approximation [34–37]. The possibility appeared to simulate X-ray scattering in crystal lattices with complex distortions. In other words, for the known character and shape of the distortion field of a crystal lattice, by solving numerically the Takagi–Taupen equations, images of such defects could be obtained in an X-ray topogram. The entire path of development of X-ray optics and topography was described in detail in three excellent monographs by Tanner [38, 39] and Authier [40]. Unfortunately, the work by Soviet and Russian scientists in this field is incompletely presented.

In our country, several research groups were simultaneously engaged in studies in this area. First of all, these are Elistratov, Efimov, and Shul'pina (Ioffe Physical-Technical Institute, St. Petersburg), Iveronova and Katsnel'son (Moscow State University, Moscow), Pinsker, Indenbom, Chukhovsky, Slobodetsky, Shtol'berg, and Koval'chuk (Shubnikov Institute of Crystallography, Moscow), Kagan, Afonas'ev, and Kohn (Kurchatov Institute, Moscow), Suvorov, Polovinkina, Smirnova, and Shulakov (Institute of Solid State Physics, RAS, Chernogolovka), Krivoglaz and Datsenko (Institute of Semiconductor Physics, Kiev), Bezirganyan and Truni (Erevan State University, Erevan), and Danil'chuk (Novgorod State University, Veliky Novgorod).

Interest in this problem was initiated to a great extent by the publication in 1965 in our country of a collection of 13 works by leading foreign researchers in the field of the electron microscopy and X-ray topography of defects in crystals. The editor of this book, Elistratov, formulated in the concluding remarks the main problems facing the study of the real structure of crystals by direct methods [41]. The most important problems pointed out by Elistratov afterwards were how the diffraction image of defects is formed in X-ray topography and electron microscopy and what information can be obtained by analyzing this image. At that time, the dynamical theory of X-ray and electron diffraction in defect crystals had only begun to be developed and, thus, these problems were extremely urgent.

The difficulty of the problem is that the wavelength λ of X-rays is comparable with the lattice parameter d: $\lambda \sim d$, whereas in visible optics $\lambda \gg d$, and in electron microscopy $\lambda < d$. The relation $\lambda \sim d$ in X-ray optics leads, according to the Bragg–Wulff equation, to large diffraction angles. As a result, each detail of the X-ray image of a defect is formed with the participation of crystal domains extended not only in the transmission direction but also in the direction of the diffraction vector — the base of the so-called Borrmann triangle (or the scattering triangle formed by the incident and diffracted beams). Because of this, each point on the input surface of the crystal always gives a band on its output surface about $2t \tan\theta$ in length, where t is the sample thickness, and θ is the diffraction angle. Therefore, images of adjacent points will overlap. For this reason, the column approximation method widely used in electron microscopy [42] cannot be applied in X-ray diffraction microscopy. The imaging of defects in X-ray topography proved to be much more complicated and diverse than that in electron microscopy. This problem was considered in detail in the review by Indenbom and Chukhovskii [43].

2. Fundamentals of X-ray geometrical optics of defect crystals

The propagation of light, radio waves, and charged particles in media with different obstacles is often described in optics by geometrical methods using the concept of the 'wave path' for determining the obstacle parameters. This is a very explicit way to describe the propagation of waves in inhomogeneous media. The necessary condition for the applicability of the geometrical approach is the relation between the size L of inhomogeneities in the medium and the radiation wavelength λ. The geometrical approximation well describes the propagation of radiation in an inhomogeneous medium if the size of the inhomogeneities greatly exceeds the radiation wavelength: $L \gg \lambda$. In this case, a very simple criterion formulated by Pierre Fermat for determining the light propagation path is used, according to which a ray propagating from one point in space to another follows the path requiring the shortest

time for its traversing. The path of rays in optics is usually described by the equations of classical mechanics (for example, the Hamilton–Jacobi equations).

Therefore, it seemed very attractive to find similar solutions for the X-ray wavelength range. However, the usual approach proves to be inapplicable for X-rays having a wavelength on the order of the inhomogeneity size. Kato [21–29], then Indenbom [44], and recently Kohn [45] have shown that the criterion of the applicability of geometrical optics for the study of X-ray diffraction in crystals is more rigid, namely, $L \gg \Lambda$, where Λ is the extinction length, the main parameter in the dynamical theory of radiation scattering by a crystal lattice:

$$\Lambda = \frac{2\pi}{\Delta k} = \frac{\lambda}{c} \frac{\cos\theta}{\sqrt{\chi_{hkl}\,\chi_{\overline{hkl}}}} \,. \tag{1}$$

Here, χ_{hkl} and $\chi_{\overline{hkl}}$ are the Fourier components of the crystal polarizability, hkl is the subscript standing for reflecting surfaces, Δk is the gap width in the dispersion surface for the exact Bragg position, and θ is the Bragg angle.

A wave field of any type (electromagnetic or corpuscular) penetrating into a crystal qualitatively changes. This new field can be described by a set of Bloch waves or, in the terms of quasiparticles, with a set of quasiparticles with different moments and masses determined by the position of the excitation point on the dispersion surface $\omega(k) = \text{const}$. The normal to the dispersion surface specifies the direction of the group velocity and, hence, the propagation direction of quasiparticles. At the boundary of Brillouin zones, the dispersion surface is split due to strong Bragg reflections. It is this region of the dispersion surface, which resembles a hyperbolic cylinder (in the two-dimensional case), that is of interest for analyzing wave fields in a crystal domain located near the Bragg reflection position. As any isoenergy surface in the inverse space, the dispersion surface is perpendicular to the Brillouin zone boundary.

In the two-wave case, the two sheets of the dispersion surface correspond to two types of Bloch waves (or quasiparticles with different signs of the effective mass and different phase velocities). The difference in the velocities of Bloch waves is determined by the splitting Δk of the dispersion surface. For the exact Bragg position, the splitting is minimum and is equal accordingly to the distance between the vertexes of hyperboles:

$$\Delta k = k^1 - k^2 \approx 10^3 \text{ cm}^{-1} \,. \tag{2}$$

If a plane monochromatic wave is incident on a perfect crystal residing in the exact Bragg position, a wave field representing a superposition of two Bloch waves is excited inside the crystal. This corresponds to the excitation of two connected points on the two sheets of the dispersion surface. In the symmetric Laue case, these points are the vertexes of hyperboles. The departure of the crystal from the exact Bragg position will result in the displacement of the excitation points along the branches of the dispersion surface and in the corresponding rotations of group velocity vectors.

Note that very small rotations of the crystal inside the dynamic reflection region (through ~ 1 angular second) roughly correspond to the rotation of the group velocity vector through 2θ inside the Borrmann triangle, i.e. a peculiar effect of 'angular amplification' with a gain of $\sim 10^4 - 10^5$ takes place during diffraction.

Omitting the details of rather cumbersome mathematical transformations, we will only outline these considerations following paper [44]. In the amplitudes of the transmitted and diffracted waves, we can separate two rapidly changing phase components corresponding to the two sheets of the dispersion surface. By substituting them into Takagi–Taupen equations, analyzing the determinant for the nontrivial solution, and using the Hamilton–Jacobi equations from classical mechanics (as is customary done in light optics), we obtain the equation for the paths of X-ray Bloch waves, which prove to be similar to the equations of motion of relativistic particles with the rest mass $\chi_{hkl}/2$ in the force field $F(x, z)$:

$$\pm\frac{\chi_{hkl}}{2} \frac{\mathrm{d}}{\mathrm{d}z} \left(\frac{\mathrm{d}x/\mathrm{d}z}{\sqrt{1 - (\mathrm{d}x/\mathrm{d}z)^2}} \right) = F(x, z) \,. \tag{3}$$

The quantity $F(x, z)$, corresponding to the force acting on a quasiparticle, is determined by the field of effective reorientations of reflecting planes of the lattice $\beta(x, z)$:

$$F(x, z) = -\frac{1}{4} \left(\frac{\partial}{\partial z} - \frac{\partial}{\partial x} \right) \beta(\mathbf{r}) \,. \tag{4}$$

The function $\beta(\mathbf{r})$ represents local deflections of the crystal lattice from the exact Bragg–Wulff condition near a defect, viz.

$$\beta(\mathbf{r}) = -2 \left(\frac{\partial}{\partial z} - \frac{\partial}{\partial x} \right) \mathbf{K_H U}(\mathbf{r}) \,. \tag{5}$$

Here, $\mathbf{K_H}$ is the diffraction vector, and $\mathbf{U}(\mathbf{r})$ is the displacement field in the crystal lattice related to the elastic field of the defect. The function $\beta(\mathbf{r})$ describes, in fact, the total local strain of the crystal lattice near the defect — local changes in the lattice parameter and the local reorientation of the lattice, i.e.

$$\delta \approx \frac{\Delta d}{d} + \Delta\theta \cot\theta \,. \tag{6}$$

Local strains caused by the diffraction of X-rays cause changes in the reflected radiation intensity, producing the image of the defect. Local deflections of the crystal lattice from Bragg–Wulff conditions (5) and (6) are called 'combined or total distortions' [46].

The two signs on the left-hand side of Eqn (3) correspond to the two signs of the mass of quasiparticles and determine the two families of paths caused by the two branches of the dispersion surface. The paths of Bloch waves in a perfect crystal are straight lines, because the field of external forces is absent, $F = 0$ (Fig. 2a). If the crystal contains elastic

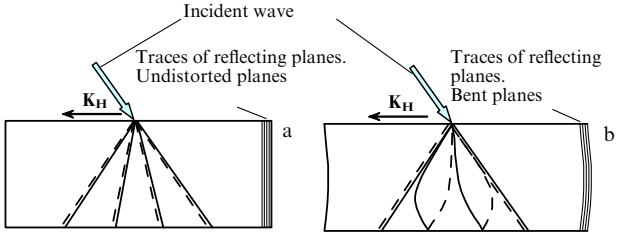

Figure 2. Schematic illustrating the paths of normal and anomalous X-ray waves in perfect (a) and deformed (b) crystals. Solid and dashed lines are the X-ray paths of weakly and strongly absorbed waves, respectively.

distortions, the ray paths undergo bending. For example, in the case of the uniform bend of reflecting planes, ray paths become hyperbolic, corresponding to the motion of quasi-particles in the constant force field $F = \text{const}$ (Fig. 2b). It is important to note that Bloch waves belonging to different sheets of the dispersion surface and having effective masses with opposite signs are deflected to different sides; for example, weakly absorbed rays are bent to the same side as reflecting surfaces. In this case, the maximum curvature of the paths exceeds the curvature of reflecting surfaces by 5–6 orders of magnitude. Ray paths, as usual, should be perpendicular to the equal-phase surfaces $S = \text{const}$.

Analysis shows that two waves propagate in the crystal: a strongly absorbed (normal) wave, and a weakly absorbed (anomalous or Borrmann) wave. The absorption coefficients for these waves are described by the expression

$$\mu_{1,2} \approx \frac{\mu}{\cos\theta}\left(1 \pm C\,\frac{\chi_{hkl\,\mathrm{i}}}{\chi_{000\,\mathrm{i}}}\cos\varphi\right). \qquad (7)$$

Here, μ is the photoelectric absorption coefficient, θ is the Bragg angle, C is a constant, $\chi_{hkl\,\mathrm{i}}$ and $\chi_{000\,\mathrm{i}}$ are the imaginary parts of the Fourier components of the polarizability, φ is the angle between the reflecting planes and the crystal surface, taking the symmetry of diffraction geometry into account. The second term in parentheses on the right-hand side of expression (7) can sometimes be close to unity and then the expression in parentheses in Eqn (7) for the normal wave becomes close to 2 (strong absorption), while for an anomalous wave it is close to zero (weak absorption). In fact, this is the Borrmann effect [47–50].

Figure 3 displays the results of computer simulation (the numerical solution of the Takagi–Taupen equations) of a wave field in the scattering triangle for a thick crystal. One can see that, as the crystal thickness grows, the normal wave is absorbed, the extinction modulations (at the vertex of the Borrmann triangle in Fig. 3a, which are shown in Fig. 3a on a large scale) cease, and a wave field consisting only of the anomalous transmitted wave begins to contract to the middle of the scattering triangle (the middle and bottom parts of Fig. 3a).

The methods of geometrical optics of Bloch waves can be applied to analyze the diffraction image in cases where the elastic field of the lattice changes smoothly enough at distances comparable with the extinction length, and the wave field has time to adjust to changes in the crystal lattice. These methods proved to be quite efficient for studying the image formation mechanisms at the edge of an oxide film [29, 52, 53], at the growth bands [54], in the far field of dislocations [55–57], etc. An analysis of Eqn (3) leads to some important conclusions concerning X-ray paths [44]:

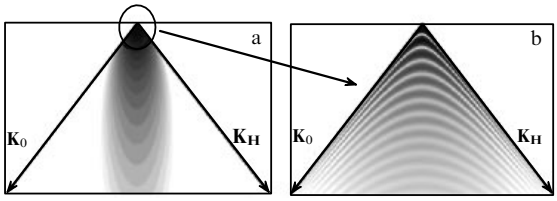

Figure 3. (a) Numerical simulation of the X-ray wave field in the scattering triangle for a thick crystal. (b) The wave field in the upper part of the scattering triangle shown in Fig. 3a, where the crystal thickness is small. $\mathbf{K}_0$ and $\mathbf{K}_\mathbf{H}$ are the wave vectors of the transmitted and diffracted waves [51].

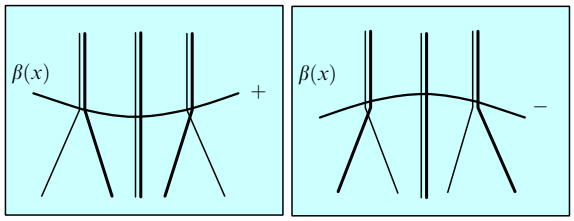

Figure 4. Focusing of the paths of normal and anomalous waves in crystals containing combined distortions of a crystal lattice in the scattering plane described by the function $\beta(x)$. The sign of the curvature of $\beta(x)$ is shown schematically. The solid and thin lines are the paths of a weakly absorbed (anomalous) wave and a strongly absorbed (normal) wave, respectively.

(i) in the absence of the displacement field, $\mathbf{U}(\mathbf{r}) = 0$, the X-ray paths will be rectilinear for any directions within the Borrmann triangle (Fig. 2a);

(ii) the strain of the crystal lattice (for example, the bend of crystallographic planes) leads to the bending of paths of the X-ray wave field;

(iii) the decrease in the displacement field along the direction of the transmitted wave will cause the deflection of weakly absorbed modes to the reflection vector, while strongly absorbed modes will be deflected to the opposite side (Fig. 2b);

(iv) the local domains of the crystal in which the function of local reorientations of the lattice in the diffraction plane has a negative curvature focus weakly absorbed rays like a converging lens; on the other hand, strongly absorbed rays are scattered as in diverging lenses. The local domains of the crystal in which the section of the function of local reorientations of the lattice by the diffraction plane has a positive curvature affect the two types of the waves in the opposite manner. This effect is schematically depicted in Fig. 4.

3. Wave field in a perfect crystal. Section topograms

The diffraction contrast in section topograms for perfect crystals is formed by the interference interaction of dynamic wave fields propagating in the crystal lattice and is determined only by the ratio of the crystal thickness to the extinction length. For the symmetric Laue diffraction, the intensity distribution on the output surface of the crystal for a point radiation source is described by the expression [43, 58, 59]

$$I(x) = \exp\left(-\frac{\mu t}{\cos\theta}\right) J_0^2\left[\frac{\pi t}{\Lambda}\,(1-\sigma^2)^{1/2}\right]. \qquad (8)$$

Here, J_0 is the zero-order Bessel function of the first kind, μ is the linear photoelectric absorption coefficient, t is the crystal thickness, θ is the Bragg angle, $\Lambda = \lambda\cos\theta/(C|\chi_{hkl}|)$ is the extinction depth, where C is the polarization factor, and χ_{hkl} is the Fourier coefficient of the crystal polarizability. The parameter $\sigma = (x/z)\,\tan\theta$ changes in the Borrmann triangle from -1 to 1. We will estimate the absorption degree by the parameter $P = \mu t/\cos\theta$. Expression (8) describes the oscillation (interference band) pattern in a topogram for the case of weak interference absorption ($P < 1$). At the center of the image, the oscillations are slow. At the edges, the oscillation frequency considerably increases upon increasing the oscillation amplitude. As the ratio t/Λ changes, the interference pattern also oscillates with a quasiperiod equal to unity.

One can see from formula (8) that the normal absorption factor $\exp(-\mu t/\cos\theta)$ defines the interference pattern intensity; however, it affects neither the mode of radiation propagation in the crystal nor the topogram contrast. The argument of the Bessel function can be utilized to estimate the change in the scattering character depending on the sample thickness: (1) $P < \pi/(3\varepsilon C)$ (thin crystal), or (2) $P > 8\pi/(3\varepsilon C)$ (thick crystal), with $\varepsilon = \chi_{hkl\,\mathrm{i}}/\chi_{000\,\mathrm{i}}$. Region 1 corresponds to interference of the wave fields, while in region 2 the contrast is determined by the anomalous transmission of X-rays. Correspondingly, the thin- and thick-crystal regions for σ polarization are determined by conditions (1) $P < 1.1$, and (2) $P > 9$. The intermediate region is characterized by a decrease in the oscillation contrast and the formation of a bell-shaped intensity distribution at the center of the Borrmann triangle. Weak oscillations in theoretical plots are noticeable for values of P up to 5.

Experimental intensity distributions obtained with laboratory X-ray sources considerably differ from theoretical predictions (8). This is explained, first of all, by the fact that radiation from X-ray tubes is nonpolarized and extinction lengths Λ for σ and π polarizations are different: $\Lambda_\pi = \Lambda_\sigma/\cos\theta$. Thus, for the Si(224) reflection of $\mathrm{MoK}_{\alpha 1}$ radiation, we have $\Lambda_\sigma = 48.3$ μm and $\Lambda_\pi = 60.7$ μm [50]. The resulting picture for nonpolarized radiation is described by the relation

$$I_{\sigma+\pi}(x) = I_\sigma(x) + I_\pi(x)\cos^2\theta\,. \tag{9}$$

Thus, the image obtained has the more complicated character, being the overlap of interference patterns for the σ and π polarizations.

Figure 5 shows three experimental section topograms for three crystals with different thicknesses, and the results of numerical simulations of the wave field of a diffracted wave in the scattering triangle in a perfect crystal [56, 60].

The second important reason for the discrepancy between experimental and theoretical intensity distributions is the exploitation of extended radiation sources for imaging. When the focal spot of an X-ray tube in the scattering plane greatly exceeds the entrance slit width, the slit itself plays the role of an extended incoherent source. The interference pattern observed in the topogram is described by the convolution of intensity distribution (9) with the transmission function of the entrance slit.

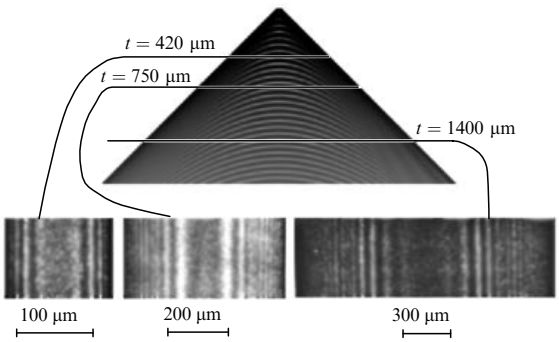

Figure 5. Experimental section topograms exemplified for crystals with three different thicknesses t (bottom), and the numerical simulation of the wave field of a diffracted wave in the scattering triangle in a perfect crystal (top) [60].

A contrast like the one described above will be blurred in projection topograms, because the structure of interference bands is not related to a certain domain of a sample.

The imaging of defects in crystals strongly depends on various diffraction phenomena. Let us consider some of them in more detail. First of all, there is the reflection of the X-ray wave field by the interface, which is called the Borrmann–Lehmann effect [61–64].

Figure 6 illustrates how the wave field interacts with the crystal–vacuum interface (the Borrmann–Lehmann effect). At the boundary, the diffraction reflection of a wave propagating in the scattering triangle appears [61–64]. The reflected wave will always consist of normal and anomalous waves. These new waves interfere with the wave field already existing in the scattering triangle, forming the image of the interface. Obviously, a similar phenomenon will take place not only at the perfect interface but also in a rapidly changing elastic field in a crystal. Therefore, this effect should play a significant role in the imaging of various defects, such as dislocations, twin boundaries, and intergrain boundaries.

Another diffraction effect playing an important role in imaging lattice defects is the focusing of an X-ray wave field. This effect, predicted by Indenbom et al. [65], was later studied experimentally [66]. The principle of such focusing is clear from Fig. 7. An X-ray beam collimated down to a width smaller than 10 μm twice diffracts in a U-interferometer. After diffraction by the first plate of the interferometer, an amplitude- and phase-modulated wave appears, which contracts after diffraction by the second plate to a thin focus. A similar effect is observed upon scattering, for example, by a stacking fault (Fig. 8) located obliquely to the crystal surface [29, 40].

Finally, we consider the field channeling along crystal lattice inhomogeneities. This effect was also predicted by Indenbom and his co-workers for a stacking fault located perpendicular to the crystal surface [67, 68] and was then

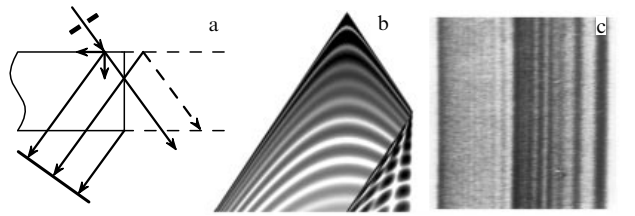

Figure 6. (a) An experimental schematic. (b) Numerical simulation. (c) Corresponding experimental section topogram [64].

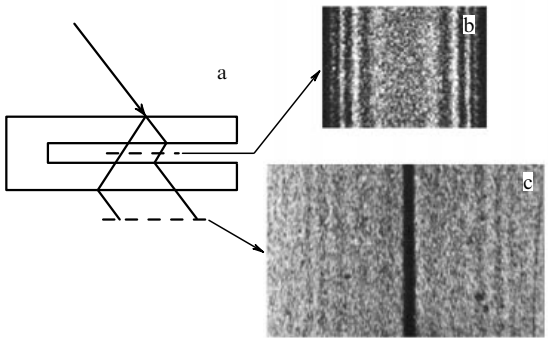

Figure 7. (a) Schematic of a double-crystal interferometer. The interferometer arms have the same thickness [66]. (b) Topogram of a diffracted wave in the first interferometer arm. (c) Topogram of a wave diffracted twice.

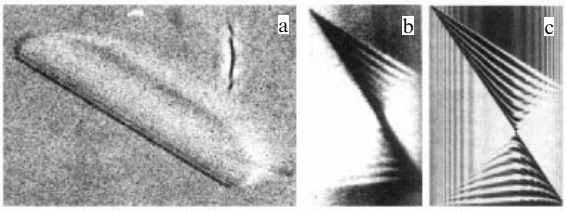

Figure 8. Diffraction image of a stacking fault in a silicon crystal (111) for the (111) CuK_α reflection. (a) Topogram obtained in the Lang scheme with scanning. (b) Section topogram. (c) Numerical simulation of the section topogram of a stacking fault [40].

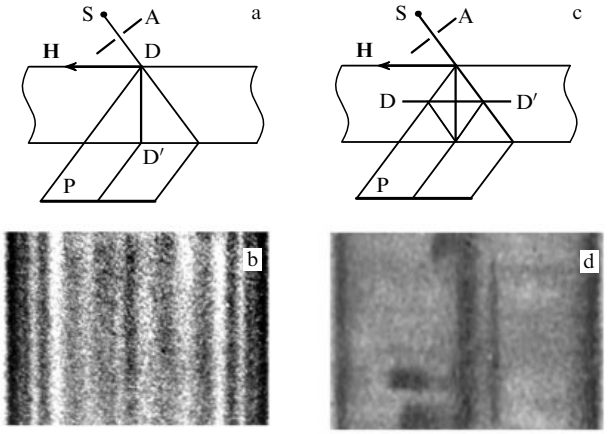

Figure 9. Disposition of a stacking fault along the bisector of the Borrmann triangle in the (111) plane (a), and the section topogram (b) produced with the use of reflection from the (333) plane, distinctly demonstrating the channeling trace along the stacking fault. (c) Disposition of the stacking fault in the (111) plane in the middle of the crystal parallel to its surface, and (d) the corresponding section (220) topogram illustrating the focusing of radiation onto the topogram center. The experiment was performed with silicon single crystals using $MoK_{\alpha 1}$ radiation [69]. A: collimator slit forming the X-ray beam, DD′: stacking fault, S: radiation source, P: two-dimensional radiation detector (photographic plate), and **H**: diffraction vector.

discovered experimentally in the diffraction of X-ray waves by crystals with stacking faults [69]. Along the stacking fault near its plane, a narrow X-ray beam propagates, i.e., the waveguide effect is observed. Figure 9 gives experimental images of the stacking fault, illustrating the channeling and diffraction focusing effects.

Naturally, all the effects considered above are tightly coupled and caused by the dynamic scattering of X-rays in crystals. It turned out that these three effects play a decisive role in the diffraction imaging of defects in X-ray topography.

4. Some aspects of diffraction image simulations

The scattering of the X-ray wave field from dislocations in crystals is commonly simulated utilizing the system of Takagi–Taupen equations [34–37]

$$\frac{\partial \psi_0}{\partial s_0} = -\mathrm{i}\pi K C \chi_{\overline{hkl}}\, \psi_{hkl}\,,$$
$$\frac{\partial \psi_{hkl}}{\partial s_{hkl}} = -\mathrm{i}\pi K C \chi_{hkl}\, \psi_0 + \mathrm{i}2\pi K \beta_{hkl}\, \psi_{hkl}\,, \tag{10}$$

where ψ_0 and ψ_{hkl} are the amplitudes of the transmitted and diffracted waves, **K** is the wave vector ($K = |\mathbf{K}| = 1/\lambda$), s_0 and s_{hkl} are the moving coordinates of the point s in the scattering plane in the coordinate system with axes representing the unit vectors $\mathbf{s}_0$ and $\mathbf{s}_{hkl}$ determining directions of the incident and scattered waves, and C is the polarization factor. The function β_{hkl} (similar to the function (5) is presented here in coordinates used in the Takagi equations) describing the local deflections of reflecting planes from the exact Bragg condition is related to the displacement field $\mathbf{U}(x, y, z)$ inside the crystal via the expression

$$\beta_{hkl} = \frac{1}{K}\frac{\partial}{\partial s_{hkl}}\,(\mathbf{HU})\,, \tag{11}$$

where **H** is the reciprocal lattice vector or the diffraction vector.

The Takagi–Taupen equations for the dislocation displacement field $\mathbf{U}(\mathbf{r})$ are commonly solved with the aid of the expression describing the field of displacements from a rectilinear dislocation in a cylindrical coordinate system [70, 71]:

$$\mathbf{U}(\mathbf{r}) = \frac{\mathbf{b}}{2\pi}\left[\varphi + \frac{\sin(2\varphi)}{4(1-\nu)}\right] - \frac{\boldsymbol{\tau}\times\mathbf{b}}{2\pi}\left[\frac{1-2\nu}{2(1-\nu)}\ln r + \frac{\cos(2\varphi)}{4(1-\nu)}\right] + \mathrm{const}\,. \tag{12}$$

Here, $\boldsymbol{\tau}$ is the unit vector of the dislocation line, $r(\varphi)$ describes the observation point around the dislocation line, **b** is the Burgers vector, and ν is the Poisson coefficient. The edge dislocation is mirror symmetric with respect to the trace of the additional half-plane. This imposes additional restrictions on the polar angle φ. We introduce the Cartesian coordinate system x_1, y_1, z_1 with unit vectors $\mathbf{e}_1 = \mathbf{b}/b$, $\mathbf{e}_2 = \boldsymbol{\tau}\times\mathbf{b}/b$, $\mathbf{e}_3 = \boldsymbol{\tau}$ for a dislocation. In this case, the angle $\varphi = \arctan(y_1/x_1)$, where the principal value of the function arctan is taken. The divergence of expression (12) near the dislocation core is removed by the choice of the coordinate origin at the center of the unit cell in a crystal. The integration constant in formula (12) is important for its interpretation. We will take it in the form

$$\mathrm{const} = \frac{\mathbf{b}}{4}\,\mathrm{sign}\,x_1\,. \tag{13}$$

Then, displacement field (12) will satisfy the boundary conditions $U_x(\infty, 0) = -U_x(-\infty, 0) = b/4$ for the dislocation model in a Peierls–Nabarro periodic medium [70, 72]. In addition, such a choice of the integration constant removes the loss of the long-range order at the periphery of dislocations in the region of $|y_1| \gg |x_1|$. Thus, significant distortions of the crystal lattice correspond to the vicinity of the dislocation line, and to the perfect matrix at the periphery. This situation is consistent with the experimental observation of dislocations in crystals.

It should be noted that the interplane distance along the y_1-axis changes in the vicinity of $|x| = d$. This distance is equal to $2d$ in the region of $y_1 \gg d$, and to d in the region of $y_1 < 0$ and $-y_1 \gg d$. Near the dislocation core, the interplane distance smoothly changes from $2d$ to d, passing through $1.5d$ at $y_1 = 0$. All this means that specular reflection from the $x_1 = 0$ interface can be observed in Bragg scattering of radiation in the region of the dislocation core.

Dislocation images were calculated by approximating system (10) with implicit second-order finite difference

equations. The boundary conditions were defined using schemes proposed in Refs [68, 73, 74]. Topograms are usually simulated taking into account the size of an extended radiation source involved in experiments, which is determined by the entrance-slit width. Because of the need for correspondence to shooting conditions, the calculated image was convoluted with the transmission function of the entrance slit. Notice that the region of the real dislocation core falls beyond the limits of applicability of the Takagi equations, and for this reason the diffraction problem is commonly simulated taking into account the core size on the order of 10 interatomic distances.

The strain region in which the Takagi equations can be applied has been studied by many authors. The results of these studies, which are most completely presented in papers [34–38], can be expressed in the form

$$\left|\frac{\partial^2(\mathbf{HU})}{\partial s_0 \partial s_{hkl}}\right| \Lambda^2 \ll 1\,, \tag{14}$$

where Λ is the extinction length. This means in practice that the radius of curvature of the ray paths should be considerably larger than the extinction length.

The intensities of diffracted and transmitted waves will be defined by the expressions

$$I_{hkl}(x,y) = |\psi_{hkl}\,\psi^*_{hkl}|\,, \quad I_0(x,y) = |\psi_0\,\psi^*_0|\,, \tag{15}$$

respectively. To calculate the diffraction image of a defect, it is necessary to find the field amplitudes and then the intensity at each point of the X-ray topogram, i.e., at the nodes (x_i, y_i) of a network dividing the entire topogram area. The intensity distribution of the diffracted wave on the output surface of the crystal in the case of nonpolarized radiation will be determined by the sum of intensities for two polarizations. Equations of this type are usually solved by the method of finite differences [34–38, 68, 73, 74]. The solution of the corresponding finite difference problem is found at network points (x_i, y_i) for each fixed value of y_j (i.e., in each scattering plane according to the chosen network) for two wave polarizations, i.e., in each section formed by the diffraction vectors $\mathbf{K}_0$ and $\mathbf{K}_1$ (of the so-called Borrmann triangle). The network step, which is usually variable, is chosen according to the required resolution of the topogram being obtained.

5. X-ray diffraction imaging of defects in crystals

The problem of X-ray diffraction imaging of defects is related to the necessity of interpreting the images of crystal-lattice defects observed in experiments. Most publications are devoted to the study of defect images in semiconductor single crystals (germanium, indium antimonide, gallium arsenide, etc.). Interest in defects was initially connected with the problems of the practical application of these materials in the electronics industry, because defects strongly affected their electric properties. Particular emphasis in the study of mechanisms of X-ray diffraction imaging in X-ray topography has been placed on defects of two types: stacking faults and dislocations.

Stacking faults pertain to planar defects with no elastic field; therefore, they are the simplest objects for diffraction studies and at the same time are of great interest, because the reflection, channeling, and focusing effects of the wave field appear on their plane [29, 40, 55, 75, 76].

Dislocations are pertinent to linear defects with a smoothly decreasing elastic field inversely proportional to the distance from the dislocation axis. In the vicinity of the dislocation axis (the dislocation core), the elastic field jumpwise changes its sign and can be approximately described by two closely separated stacking faults with opposite signs. This case is more complicated than that of a stacking fault. However, it is most interesting because, here, various interactions of an X-ray wave with the elastic field are realized: first, the interaction of the wave with a continuously decreasing elastic field when the ray optics can be employed; second, the interaction with the rapidly changing elastic field near the dislocation axis where the elastic field changes its sign. Therefore, below we will mainly discuss the contrast of dislocations, because all the varieties of interactions of the X-ray wave field with the complex elastic field of defects are observed namely for dislocations.

The first systematic concepts of the X-ray diffraction imaging of dislocations were presented by Authier [12, 40, 75, 76]. Figure 10 demonstrates a dislocation located obliquely to the sample surface. Authier's terminology applied to various details of the image is presented in the figure caption.

The dislocation image in Auther's work was conventionally divided into three parts: the 'direct' or 'kinematic' image formed in the strongly distorted region of the dislocation elastic field, because the incident beam has a finite divergence and a certain spectral composition; the 'dynamic' image related to dynamic diffraction effects, and, finally, the 'intermediate' image produced due to interference of the light field propagating in the Borrmann triangle with new wave fields appearing in the distorted region near dislocations [12, 40].

Subsequent experimental and theoretical studies showed that the fundamental principles of the dislocation contrast

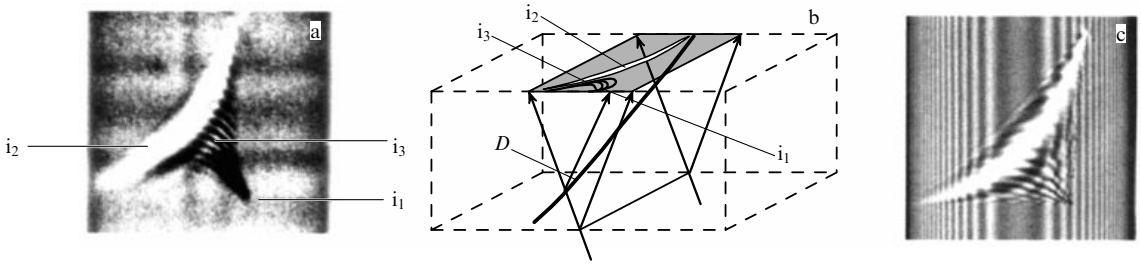

Figure 10. (a) Experimental section image of the dislocation D located obliquely in a silicon sample in the form of a parallelepiped; $MoK_{\alpha 1}$ radiation, a 0.8-mm thick crystal, and $\mu t = 1.12$, (220) reflection. (b) Schematic view of a defect crystal: i_1 — direct image, i_2 — dynamic image, and i_3 — intermediate image. (c) Numerical simulation of the section topogram corresponding to Figs 13a, b [12, 40].

proposed by Authier correspond to reality as a whole; however, the real picture of X-ray imaging of dislocations is more complicated [55, 63, 64, 76–86].

The kinematic contrast is related to considerable variations in the interplane distance and the orientation of reflecting planes near the defect core. As a result, the angular and chromatic spectra of the incident wave corresponding to the scattering of incident radiation in the distorted region prove to be considerably broader. In other words, the fraction of the incident beam scattered in the distorted region of the crystal greatly exceeds the fraction of the beam scattered in perfect parts of the sample, and the kinematic image is drastically distinguished in its intensity in the topogram. The kinematic image is transferred to the output surface of the sample with normal absorption along the propagation direction of the diffracted wave. In fact, the kinematic image presents the 'direct' image of the strongly distorted region. It is connected to the local region of the sample and is reproduced correspondingly in scan topograms. Thus, the kinematic contrast corresponds to the strongly distorted region near the dislocation core, while the dynamic interference image of the defect is formed at the periphery in the region of weak lattice distortions.

The phenomena taking place upon X-ray scattering by a crystal lattice distorted by the elastic dislocation field strongly depend on the strain gradients. Away from dislocations, where the elastic field of the lattice changes weakly enough at distances on the order of the extinction length, the wavefield energy flux has time to adjust to changes in the crystal lattice. In this case, the main mechanism forming a dislocation image, if these processes are described in the language of ray trajectories, will be the displacement of the trajectories of Bloch waves, the change in their phases, and their interference. This results in forming the dynamic image. The dynamic contrast of defects in section topograms is revealed in the form of the interference band pattern around the direct image of the defect. In projection topograms, a contrast of this type will be blurred, because the geometry and structure of these bands depend on the location of the defect under the Borrmann triangle. Dynamic interference bands, which are very sensitive to the crystal perfection degree, are determined by stresses (more exactly, by the displacement field) caused by defects. Thus, for a dislocation density above 10^3 cm^{-2}, interference bands virtually disappear.

Dislocation lines in single crystals usually have a quite peculiar shape and orientation and, therefore, analysis of the contrast of such dislocations, in general, is complicated. This problem can be solved, as a rule, only for special orientations of dislocations, namely when their axis is parallel to one of the preferential directions in the crystal: the directions of the diffraction vector, the normal to the scattering plane, and the direction perpendicular to the first two, i.e., when the dislocation axis lies in the scattering plane perpendicular to the diffraction vector. These orientations were called the 'special positions' of the defect. This approach was proposed by A M Elistratov in his concluding editor's remarks to book [41]. The term 'special position' was first used in paper [81].

To perform analysis and simulations, any general spatial location of a defect can be divided into small rectilinear parts, then these parts are decomposed into three components along the directions mentioned above, and the three corresponding problems are solved. Therefore, to understand how imaging occurs, it is appropriate to study the imaging of dislocations for these orientations and to construct the corresponding scattering models for them. This approach was applied for studying the mechanisms of dislocation imaging [82, 83–91]. The idea of this approach is schematically illustrated in Fig. 11.

By comparing the images of dislocations in different orientations in the scattering triangle (Borrmann triangle), one can distinguish different interference effects involved in the X-ray diffraction imaging of dislocations and estimate their role [37–39, 82, 83–91]. In Sections 5.1–5.3, we will present experimental images of dislocations in special positions and the results of numerical simulations of these images and analyze mechanisms involved in the formation of the diffraction contrast. The results described in Sections 5.1–5.3 are obtained for rectilinear dislocations. The method for producing such dislocations was described in paper [82].

5.1 Dislocation line perpendicular to the scattering plane

Consider the case with the dislocation axis perpendicular to the scattering plane [80, 82–95]. Figure 12 shows the experimental setup, experimental section topograms, and the corresponding results of numerical simulation. The rectilinear 60° dislocation D is located perpendicular to the scattering plane. A sample can be displaced by dint of the X-ray beam by a strictly fixed distance multiple of 10 μm. Thus, section topograms are obtained with different dispositions of dislocation lines in the scattering triangle.

The dislocation in Fig. 12b is located in the left part of the Borrmann triangle and intersects the propagation direction of the incident beam. In Fig. 12c, the dislocation is located approximately in the middle of the left part of the Borrmann triangle.

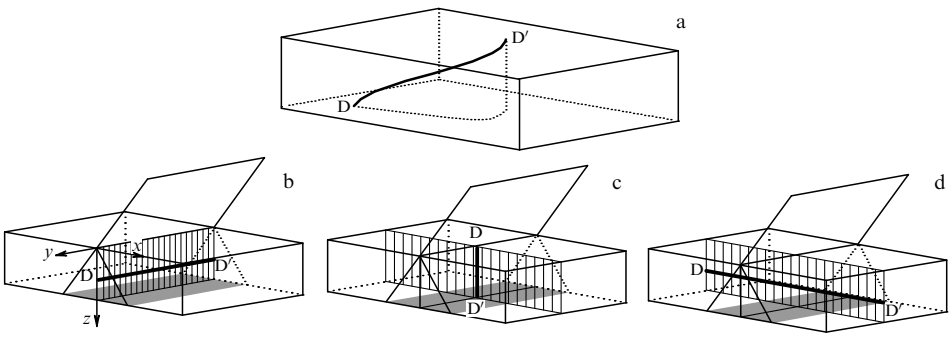

Figure 11. (a) General disposition of the curvilinear D – D′ dislocation. Special positions of the dislocation: (b) the dislocation axis is perpendicular to the scattering plane, (c) the dislocation axis lies in the scattering plane perpendicular to the reflection vector, and (d) the dislocation axis lies in the reflection plane parallel to the diffraction vector [85].

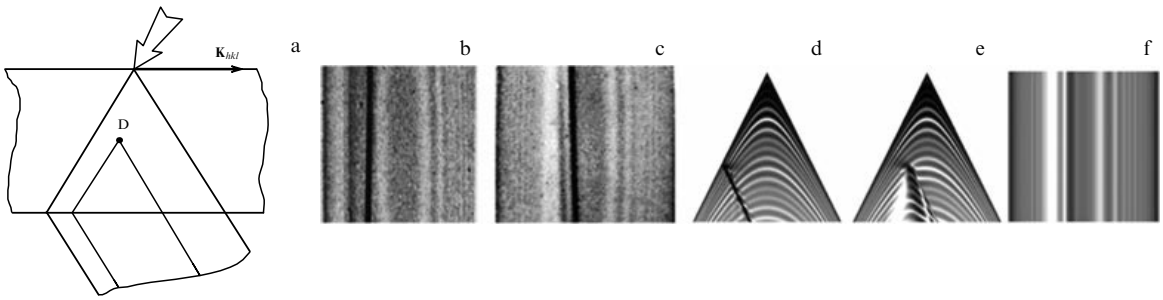

Figure 12. (a) Setup of the experiment. (b) Part of the section topogram with a dislocation located at the edge of the scattering triangle ($x = -152$ μm). (c) Part of the section topogram; the dislocation is located in the left part of the scattering triangle; $x = -57$ μm (distance is measured from the bisector of the scattering triangle). (d, e) Numerical simulations of the wave field in the scattering triangle corresponding to figures b and c. (f) Section topogram corresponding to figure c [80]. A silicon single crystal, a 60° dislocation at a depth of 565 μm, $MoK_{\alpha 1}$ radiation, and crystal thickness $t = 730$ μm.

It is of interest to consider the behavior of the wave field inside the scattering triangle. Reflecting planes are perpendicular to the input surface of the sample and the plane of Fig. 12b. The 60° dislocation lies perpendicular to the plane xy of the figure and the dislocation line is directed along the y-axis. The edge component of this 60° dislocation has the Burgers vector $\mathbf{b} = (b_x, 0, b_z)$. Therefore, the screw component in this diffraction geometry does not contribute to the dislocation image. The image is only determined by the edge component. Wave field distributions over the scattering plane are shown in Figs 12d and 12e. Figure 12d clearly demonstrates the projector of the direct image from the region of intersection of the direct beam with the strongly distorted region of the dislocation core. Note the absence of the bright direct image of the dislocation in Figs 12c and 12e. This is explained by the fact that the dislocation core is located outside the primary beam. On the other hand, the peripheral regions of the dislocation considerably perturb the dynamic interference pattern. Analyses of experimental section topograms and calculated images show that the structure of the dislocation image in the case of section topograms strongly depends on the site where the dislocation intersects the scattering triangle.

A direct or kinematic image of a dislocation in section topograms is only present when the strongly distorted region near the dislocation core with a rapidly changing reorientation field intersects the incident light beam. In this case, a bright projector appears in the direction of the diffracted beam from the region of the incident beam intersection with the dislocation axis. The direct image of the dislocation in the section topogram allows one to determine its level depth under the sample surface.

As the dislocation line moves away from the primary X-ray beam axis, the projector brightness rapidly decreases, the scattered beam splits into numerous interference spots, and a light shadow related to the redistribution of the wave scattered in a weakly distorted region appears near it on the side of the primary beam.

Consider another very important mechanism responsible for direct imaging. The function of effective reorientations near the dislocation core very rapidly changes as the dislocation axis is approached, then goes out outside the reflection curve, and a local region near the core simply becomes an absorbing material for the incident X-ray wave. Thus, a region exists around the dislocation axis where the X-ray wave field barely interacts with the crystal lattice. Therefore, a pseudoboundary appears from which the X-ray wave should be scattered, as in the case of a bounded crystal, i.e., reflection will appear as from a mirror surface, the only difference being that normal and anomalous waves are formed each time. The emergence of new waves during the interaction of the propagating wave with the interface was called *interbranch scattering* in the literature [38–40].

Here, an analogy exists with radiation scattering from the interface in a bounded crystal — a strongly distorted region of the elastic strain field near the dislocation core is similar to a semitransparent mirror from which a part of the perfect crystal wave field formed inside the scattering triangle is reflected [61–64]. This reflected field is coherent to the primary field because it is produced by the latter and, hence, the reflected field interferes with the primary wave field, forming the observed diffraction image of the dislocation.

The mechanism described above is confirmed by the results of paper [85]. Consider the model of a crystal lattice harboring a defect in the form of a thin rectilinear tube about 1 μm in diameter whose material does not reflect X-rays, and its interaction with an X-ray wave is reduced to photoelectric absorption. This model completely excludes the influence of the decreasing elastic field of a dislocation ($\sim 1/r$) on imaging and can be applied to studying the physics of direct imaging of defects. Let us simulate numerically this situation. In this model, the region of interaction of the wave field in the scattering triangle is localized, being bounded by a section through the model tube passed by the diffraction plane.

All scattering processes occur here in the line of the section through the model tube passed by the scattering plane. From this region, a bright projector appears in the diffracted beam direction. This beam is just a direct image of our model of the defect. It is formed due to scattering from tube walls, as this occurs in a bounded crystal [61–64]. Figure 13 depicts diagrams of the numerical experiment and the corresponding section topogram and scattering triangle [85]. Inside a triangle formed by the incident beam direction and the ray forming the direct image, interference naturally occurs between the old wave field and the new one produced due to the scattering of the main wave field by the tube walls. This process is illustrated in Figs 13b, c.

All these subtle details of the image are averaged in constructing topograms with scanning, and only a bright trace of the direct image and a weak light shadow remain.

5.2 Dislocation line located in the scattering plane parallel to the reflection vector

The case in which the dislocation line is located in the scattering plane parallel to the reflection vector is of special interest, because it is a particular one-dimensional case in

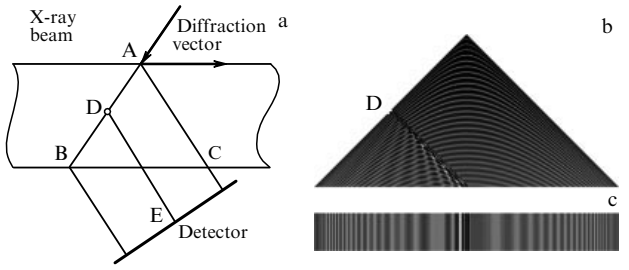

Figure 13. (a) Diagram of a numerical experiment for a crystal harboring the defect D in the form of a thin rectilinear tube around 1 μm in diameter perpendicular to the scattering plane. The tube material is completely out of the reflection position. ABC: the Borrmann triangle, E: the trace of the direct defect image. (b) Wave field in the Borrmann triangle. (c) Corresponding section topogram [85].

studies of thin near-surface layers in single crystals used in microelectronics, optoelectronics, and X-ray optics. In this event, dislocations are only a convenient model for studying the scattering of the X-ray wave field by localized deformations in real crystals.

5.2.1 Dislocation imaging in a thin crystal. Figure 14 demonstrates the experimental geometry and section topograms for three diffraction powers of dislocations [51, 55, 57, 77, 86–88]. The dislocation axis in this geometry intersects the whole scattering triangle along the diffraction vector and, therefore, all the points of the defect lying in the scattering plane will contribute to the defect image formed on the output surface, as shown in papers [38, 40]. Each point in the strongly distorted region near the defect axis will produce new wave fields, as occurs at the crystal–vacuum interface [61–65]. In other words, each point on the defect axis becomes a source of scattered waves, i.e., a new scattering triangle is formed at each point and a complex defect image, being the superposition of all scattered waves, will be formed on the output surface of the crystal [43, 55, 56, 95].

Experimental section topograms display that the image shape becomes more complicated upon increasing the parameter m: (1) the bend of interference bands increases and new interference bands appear, and (2) the size of the direct image increases and its shape is complicated. This result was analyzed in detail in paper [55] within the framework of geometrical optics.

The paths of normal and anomalous waves propagating in the crystal lattice near dislocations bend in the elastic field and acquire the additional path difference and, hence, the additional phase difference.

Figure 15 presents schematically the surface of an additional phase difference appearing during the propagation of waves in the elastic dislocation field. The figure demonstrates the formation mechanism of new interference maxima and the bend of already existing bands. Obviously, this bend is caused by the additional path difference of beams in the elastic dislocation field.

Figure 16 exhibits the function of local disorientations for the screw dislocation shown in Fig. 14. The field was calculated following the expression

$$\beta_{\mathbf{H}}(y,z) = \frac{1}{K}\,\frac{\mathbf{Hb}}{2\pi}\,\frac{y}{y^2+z^2}\,,$$

where **H** is the diffraction vector, and **b** is the Burgers vector.

The contrast formation mechanism described above operates only in the far field of the dislocation, when crystal distortions continuously change over the extinction length, which is determined by the splitting of the dispersion surface near the Bragg reflection. In this case, the wave field has time to adjust to changes in the crystal lattice and, therefore, the ray optics approaches can be employed.

If changes in the elastic field of the defect over the extinction length are considerable and local disorientations exceed the reflection curve width (i.e., $\beta(r) \geqslant |\chi_{hkl}|$), the wave field has no time to follow changes in the crystal lattice, the diffraction of waves by strong crystal distortions takes place, and interbranch scattering appears. In this case, each wave will produce a whole family of new Bloch waves interfering with each other and the already existing wave field, which considerably complicates the analysis of scattering mechanisms [85]. It is in the regions near the dislocation axis, where the function of local disorientations of reflecting planes quickly changes its sign, that the direct (kinematic) image of the dislocation is formed. As the diffraction power m of the defect increases, the size of the direct image increases and its fine structure is beginning to emerge. This is caused by the increase in the dimensions of the strongly distorted region around the dislocation axis.

Figure 17 demonstrates three section topograms for large diffraction powers of a defect, which highlight the fine

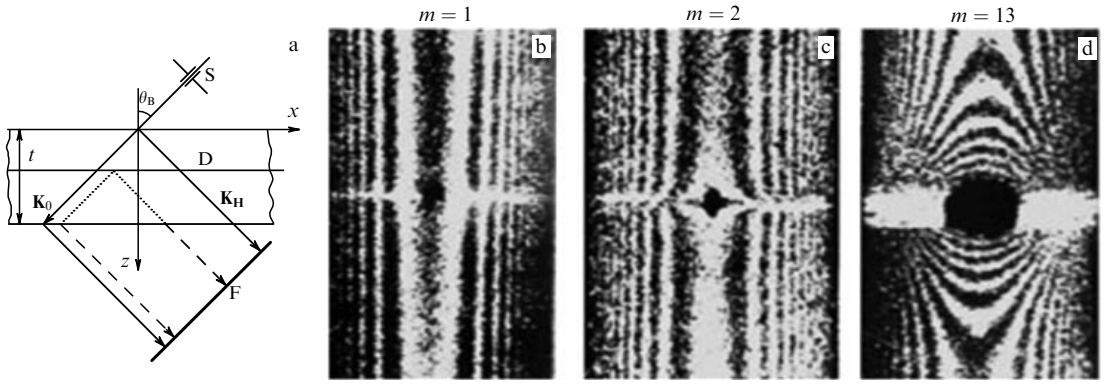

Figure 14. (a) Setup of the experiment. S: forming collimator slit, F: direct image of the dislocation D on a detector, θ_B: the Bragg angle. (b–d) Section topograms with dislocation images with different diffraction powers $m = \mathbf{K_H b}/(2\pi)$ of the elastic distortion field. The crystal thickness is $t = 410$ μm, $MoK_{\alpha 1}$ radiation, reflection from the (220) planes. All dislocations are helical; the Burgers vector is oriented along the diffraction vector **H** [88].

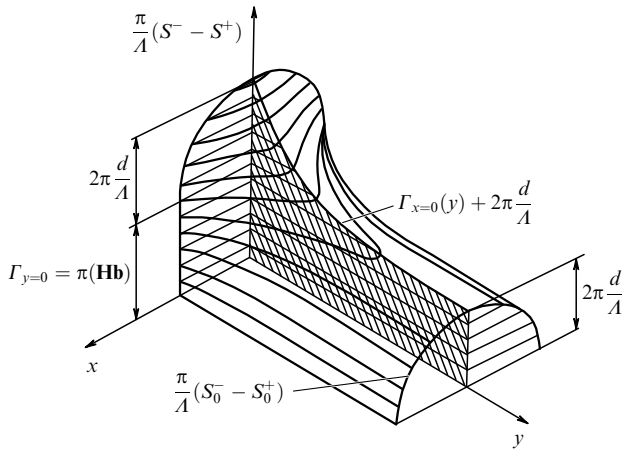

Figure 15. General view of the total-phase-difference surface for waves in the elastic field of the dislocation. S^+ and S^- are phases of two types of Bloch waves propagating in the scattering triangle, Γ is the phase difference for these waves, Λ is the extinction length, **H** is the diffraction vector, **b** is the Burgers vector, and d is the interplane separation. Horizontal lines correspond to extinction bands in section topograms [55].

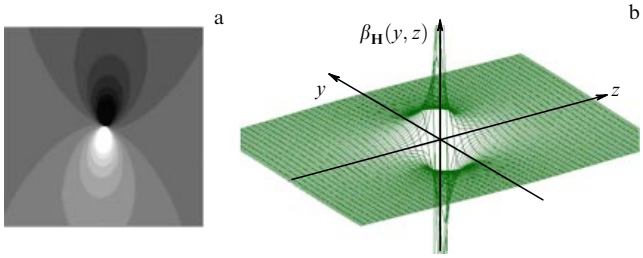

Figure 16. Function of effective local disorientations of a reflecting plane for one screw dislocation: (a) projection on the yz plane, and (b) three-dimensional view of the function of local disorientations. The vector **H** corresponds to reflection from the $(0\bar{2}2)$ plane [84].

structure of the direct image. The formation of such a complex direct image is explained by the interaction of the strongly distorted region near the dislocation axis, where the function $\beta(r)$ changes sign, with the interference maxima of the wave field formed in the scattering triangle [85, 86, 89, 90]. At each point where the strongly distorted region near the dislocation axis intersects interference bands of the hyperbolic shape, new waves appear due to interbranch scattering. These waves interfere with the wave field already existing in the scattering triangle. As a result, a complex direct dislocation image with the developed fine structure is formed.

Figure 18 gives the result of numerical simulation of the wave field in one of the sections of the scattering triangle ($y = 0$) and the corresponding section topogram. The section topogram consists of a few hundred such sections (-200 μm $< y <$ 200 μm).

It is important that the shape of the elastic field for each fragment of the dislocation and its orientation rather weakly affect the character of a new X-ray wave field. The strongly distorted region near the dislocation core interacting with the X-ray wave field in the scattering triangle plays the role of an X-ray mirror. A new wave field appearing in a new scattering triangle coherently interacts with the old field producing the X-ray image. At the same time, the general form of the contrast will be determined by the form and orientation of the dislocation line, because each newly formed wave field propagating from a certain point of the scattering triangle has its own initial phase. It is the summation of these waves, taking their phases into account, that leads to such a great variety of defect images.

To explain qualitatively the observed images shown in Figs 15 and 16, the near dislocation field can be approximately considered, according to Refs [64, 66, 67], as the field produced by two closely spaced stacking faults. In this case, the newly produced wave field under the dislocation will be similar to the field appearing in the case of a stacking fault [29]. This means that the image of the near field of dislocations will consist of two parts: a dynamic oscillating shadow formed by the diverging cone of rays under the dislocation, and the diffraction focusing of rays of a new wave field being formed by the converging bundle of paths [64].

The above approach is confirmed by the results of numerical simulation with the involvement of the hypothetical model of a dislocation in the form of a tube whose material came out from the reflecting position [85]. Consider a geometry in which the defect axis is parallel to the diffraction vector and lies in the middle of the crystal thickness. Analysis of the simulated results shows that both the scattering triangle of the wave field and the numerical topogram of this model virtually coincide with the corresponding images obtained in the case of the usual screw

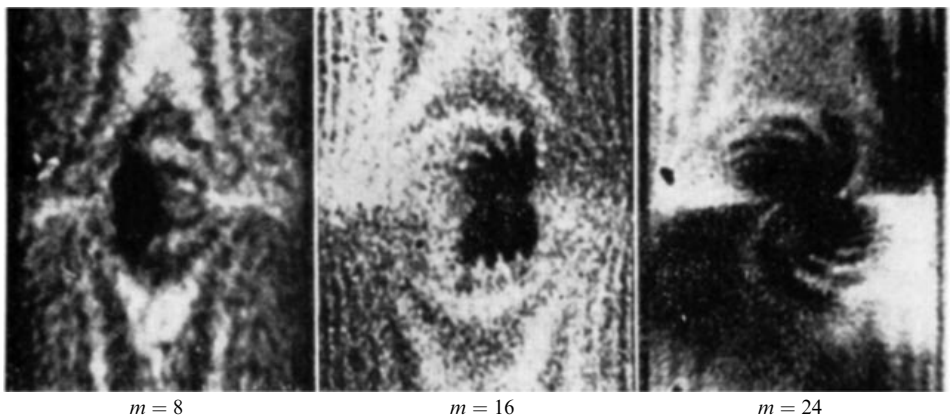

Figure 17. Experimental section topograms of the same screw dislocation for diffraction powers $m = 8$, 16, 24. The silicon crystal thickness is 410 μm; (220), (440), and (660) reflections, and $\mathrm{MoK}_{\alpha 1}$ radiation [55].

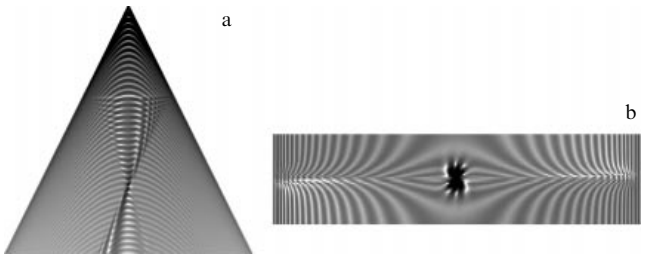

Figure 18. (a) Simulated section of a wave field in the scattering triangle at $y = 0$, and (b) the corresponding section topogram [85].

dislocation, when its axis coincides with the direction of the diffraction vector [88]. The direct image of the model tube in the scattering plane is formed due to the diffraction interaction of new and old wave fields at the interface [61–64]. Thus, the direct image formed in this geometry stems from the superposition of all the wave fields generated at points of the tube interface. A similar phenomenon is observed, for example, in stacking faults or in a double-crystal X-ray interferometer. This effect was called the *X-ray diffraction focusing* [65, 66]. It is this result that we fix in the form of a direct image of a defect in a section topogram.

The experimental and simulated results considered in this section show that the imaging of a dislocation involves all points on the dislocation axis or, more exactly, all points in the strongly distorted region near the dislocation core falling inside the scattering triangle. Each such point is a source of a new propagating wave field. The interference of all these fields forms the dislocation image. The brightest part of this image – the direct image — is formed in the region of the intersection of the dislocation axis and the incident beam direction (Fig. 19).

Cases are also known when the direct image is absent in the section image of a defect [84, 91, 92]. For example, this is shown in Fig. 20 demonstrating the image of a macrodefect ≈ 250 μm in size in a silicon single crystal doped with phosphorus up to a concentration of 7×10^{19} cm^{-3}. The direct image does not appear because local distortions of the crystal lattice are small and do not come out from the Bragg reflection region. Similar images of a larger size were also observed in Ref. [96].

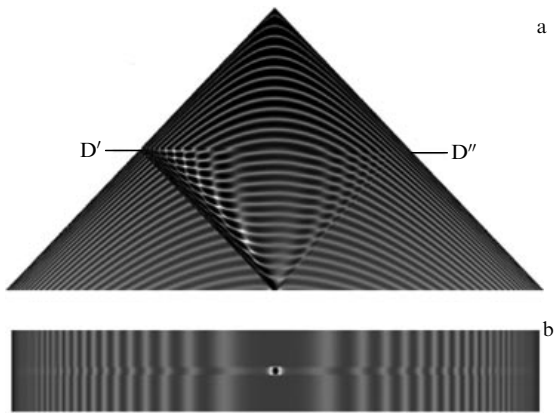

Figure 19. (a) Simulated scattering triangle, and (b) the corresponding section topogram. A defect with the D′D″-axis in the form of a thin tube, whose material is out of the reflecting position, is located parallel to the diffraction vector in the middle of the crystal over its thickness in the scattering plane. The crystal thickness is 1000 μm; calculations were performed for $MoK_{\alpha 1}$ radiation reflected from (220) crystallographic planes [85].

5.2.2 Dislocation imaging in a thick crystal. Let us consider the mechanism of dislocation imaging in a crystal when the normal wave is completely absorbed, i.e., $\mu t \gg 1$, and the whole contrast is formed only by the anomalous wave. Figure 21a exhibits the typical section topogram of a screw dislocation oriented along the diffraction vector [78]. The topogram demonstrates a light shadow under the dislocation. Interference bands are naturally absent in the topogram. The intensity distribution in the transverse direction possesses a bell shape.

Notice that the light shadow strip of the dynamic image is displaced upward and downward on each side of the image. This effect is probably explained by the asymmetric displacement of paths for the normal and anomalous modes of the wave field on each side of the dislocation along the coordinate y observed earlier in paper [55]. Because absorption for the normal and anomalous modes of the wave field is different,

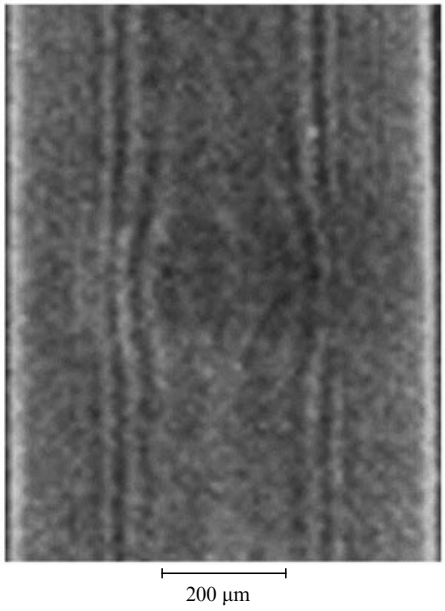

Figure 20. Fragment of the section topogram of silicon with the image of a macrodefect. Silicon is doped with phosphorus up to 7×10^{19} cm^{-3} level, MoK_{α} radiation, and (440) reflection [84].

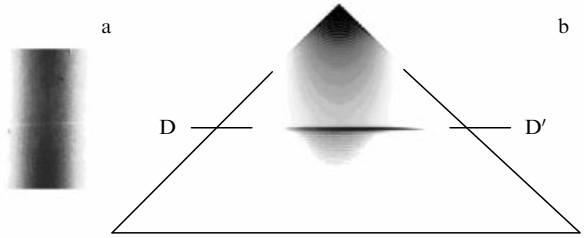

Figure 21. (a) Experimental section topogram of a silicon single crystal with the image of a screw dislocation. The crystal thickness is 800 μm, $\mu t \simeq 15$, $CuK_{\alpha 1}$ radiation, and (220) reflection. The dislocation axis is oriented along the diffraction vector. (b) The simulated wave-field distribution in the scattering triangle for the case presented in figure a. The dislocation axis is located in the middle of the crystal thickness [83].

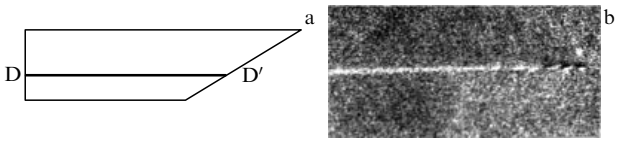

Figure 22. (a) Diagram of a wedge crystal with the DD′ dislocation. (b) Experimental X-ray topogram obtained by the Lang method with scanning [51].

the distribution of the total wave field in the scattering plane will be asymmetric.

Figure 21b presents the wave field distribution in the scattering triangle for a thick crystal. One can readily see that extinction oscillations gradually decrease over the crystal depth during the absorption of the normal wave. The whole waveguide field contracts to the bisector of the Borrmann triangle. Only the anomalous wave reaches the dislocation axis. During the interaction of this wave with the strongly distorted region of the crystal near the dislocation axis, a new wave field appears due to interbranch scattering. This wave field again consists of normal and anomalous waves and extinction oscillations again appear. The normal component is gradually absorbed during its propagation into the crystal, and only the anomalous Borrmann wave remains again. In this case, approximately half the field energy is spent to form the normal wave due to interbranch scattering. Because of this, the anomalous component reaching the output surface of the crystal under the dislocation will be attenuated by half, producing the image contrast in the form of a light shadow in section and scanned topograms. This imaging mechanism is illustrated in Fig. 22 showing a scanned topogram obtained on a wedge silicon crystal. Oscillations in the thin part of the wedge demonstrate the formation of new waves.

This example once more emphasizes that each point of the strongly distorted region near the dislocation core falling within the wave field propagating in the scattering triangle becomes a source of a new wave field, i.e., a new scattering triangle will appear.

5.3 Dislocation line located in the scattering plane perpendicular to the reflection vector

5.3.1 Dislocation imaging in a thin crystal (weak absorption). We will consider below experimental topograms and the results of numerical simulations obtained for a thin crystal [93]. This case is of interest because, here, the dislocation line intersects the scattering triangle and, therefore, new wave fields will appear at each point of the strongly distorted region of the elastic dislocation field within the scattering triangle [43, 93–95], which interact not only with each other but also with the primary beam. Because the crystal is thin, all the new waves reach the output crystal surface.

Figure 23 displays the experimental setup, the two typical experimental section topograms demonstrating the details of the X-ray diffraction image of the dislocation perpendicular to the input surface of the crystal, and the corresponding simulated results. These topograms were obtained for two positions D_1 and D_2 of the dislocation in the scattering triangle: in the first case, the dislocation intersects the incident beam direction approximately in the middle of the left side of the scattering triangle (Fig. 23b), while in the second case it is located almost along the bisector of the scattering triangle (Fig. 23c).

The bright strip normally intersecting interference bands attracts attention (Fig. 23b). It portrays the direct image of the dislocation forming in the vicinity of the intersection of the strongly distorted region near the dislocation axis with the primary beam. The image is inhomogeneous along its length. As the dislocation line moves inside the scattering triangle, the direct image region moves along the base of the scattering triangle from the left edge (Fig. 23a, the end of vector $\mathbf{K}_0$) through the center of the scattering triangle to its right part (to the end of vector $\mathbf{K}_1$). During this motion, the image brightness gradually decreases. When the dislocation axis passes along the vertical bisector of the scattering triangle, a bright image appears in the middle of the base of the Borrmann triangle, which is especially well observed in Fig. 23c. Along with these bright details of the image, the photographs distinctly demonstrate light regions of the geometric shadow to the left of the dislocation. The elastic field of the dislocation sort of casts a shadow in the direction of the incident beam. An analysis of experimental topograms and calculated sections of the wave field in the scattering plane shows that the dislocation imaging in such a geometry resembles the case of diffraction in a bounded crystal [61–64]. Figures 23d, e present the results of numerical simulations of fragments of the section topograms shown in Figs 8a, b. The images correspond rather well to experimental section topograms.

Figures 23f, g exhibit the intensity distributions in the scattering triangle calculated via Takagi equations for two dislocation positions D_1 and D_2. The wave-field intensity distributions in the scattering triangles clearly demonstrate

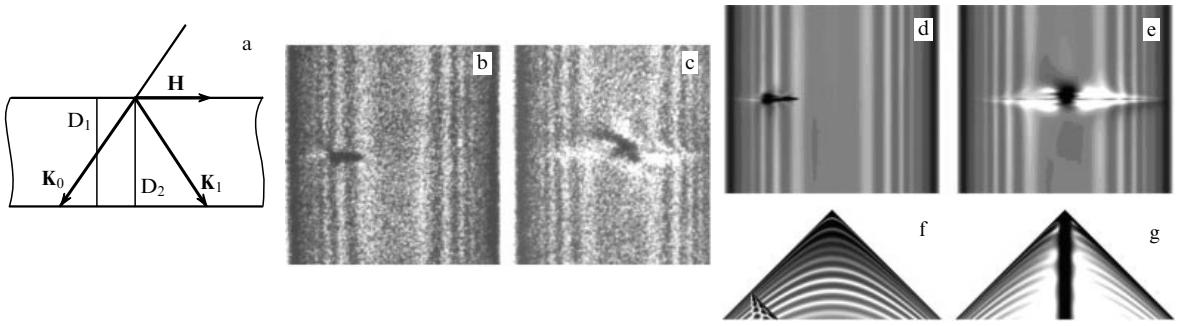

Figure 23. (a) Setup of the experiment. (b, c) Experimental section topograms. (d, e) Calculated section topograms for cases in figures b and c. (f, g) Corresponding wave fields in the scattering triangle for the same cases. The silicon crystal thickness is 450 μm, $MoK_{\alpha 1}$ radiation, and (220) reflection [94].

the topographic imaging due to wave-field reflection from the strongly distorted region near the dislocation axis, similar to reflection from the interface in the case of a bounded crystal. Figure 23g illustrates the wave-field formation in the form of an oscillating bundle in the near field of the dislocation.

Let us consider some salient features of the observed images. The images obtained by numerical simulation more distinctly reveal the reflection effect of the wave field in the near field of the dislocation than experimental images do. This effect, which is manifested in oscillations of the contrast adjacent to the direct image (Fig. 23f), is analogous to the wave-field reflection effect from the sample edge in the Borrmann triangle [61–64]. It seems that the region separating a strongly distorted part of the crystal from the region with a smoothly changing of elastic fields in this case play the role of a peculiar interface inside the crystal. This explains the analogy with a bounded crystal.

The second interesting effect is shown in Figs 23c, e, where the higher concentration of the wave field is seen near a strongly distorted region of the defect in the event when the dislocation axis coincides with the bisector of the scattering triangle. This effect is probably analogous to the interference effect of wave-field focusing in crystals with an ultrasonic field, which we observed earlier [95]. A similar effect was also described by Indenbom et al. [67, 68] for X-ray scattering by stacking faults, where the phase of scattered waves changed by π. However, this effect was experimentally observed only for stacking faults [69].

It seems that the diffraction effect concentrating the wave field in a strongly distorted region in the near field of the dislocation [94] is related to wave-field channeling. The latter can be qualitatively described if we assume that the strongly distorted crystal region near the dislocation axis represents a part of the crystal that leaved radiation reflection. Then, the parts of the wall of such a tube located in the scattering plane should operate due to multiple reflections like a slitless collimator, as proposed back in the 1960s in papers [96–98].

The channeling effect in the 'purest' form was described in paper [85] by simulating diffraction by a crystal containing inside a thin $D'D''$ tube oriented perpendicular to the crystal surface, the material of the tube having leaved the reflection position. The results of this numerical experiment are presented in Fig. 24.

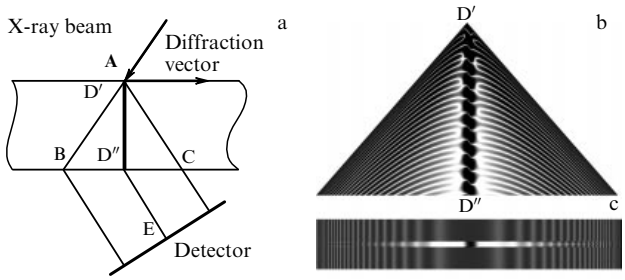

Figure 24. (a) Diffraction schematic. The sample contains a region in the form of a thin $D'D''$ tube whose material is outside the reflecting position. (b) Simulated wave-field distribution in the scattering plane, and (c) the corresponding section topogram [85].

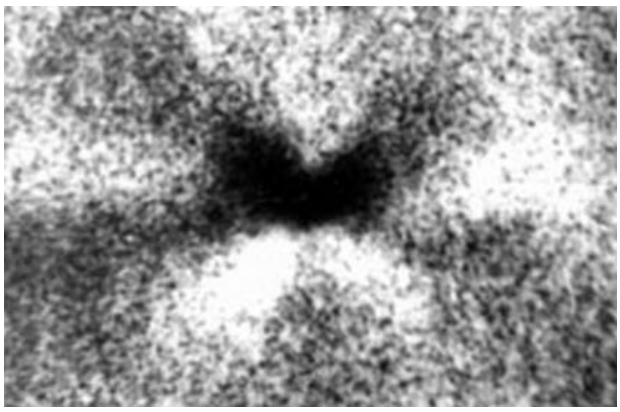

Figure 25. Image of the edge dislocation perpendicular to the sample surface. The dislocation axis is parallel to the [110] direction; (220) reflection; $CuK_{\alpha 1}$ radiation, $\mu t = 20$.

5.3.2 Dislocation imaging in a thick crystal (strong absorption). X-ray images of edge dislocations perpendicular to the crystal surface were studied in silicon single crystals in papers [99–101]. A typical topogram with the image of the 60° dislocation is exhibited in Fig. 25.

The topogram was obtained following the Borrmann scheme in a broad beam. A comparison of the experimental image with the rosette of effective disorientations for the edge dislocation shows that they coincide as a whole (see Fig. 25). However, some differences exist as well. The experimental image reveals some details that are absent in the rosette of effective disorientations. First, the experimental topogram exhibits horizontal black and white lobes to the left and right along the horizontal axial line. Second, two lobes are clearly seen along the vertical middle line of the image: a light lobe in the upper part, and a dark one in the lower part. Such details are absent on the map of the function of local disorientations (see Fig. 27).

Because of this, the images of edge dislocations were studied by section topography methods [93–95]. Figure 26 displays the section images of edge dislocations perpendicular to the surface of silicon crystals for the two orientations of a dislocation position in the crystal: (1) the reciprocal lattice vector is parallel to the Burgers vector, Si $(2\bar{2}0)$ reflection, and (2) the reciprocal lattice vector is perpendicular to the Burgers vector, Si (004) reflection, and also corresponding topograms calculated for three dislocation positions in the scattering triangle.

For these two dislocation orientations, the sets of section topograms were obtained with dislocations located in different parts of the scattering triangle for $CuK_{\alpha 1}$ radiation. The topograms were obtained for one 1810-μm thick sample for the same dislocation [102, 103].

From the point of view of the variety of diffraction effects, the most interesting was orientation (1). Therefore, we will consider this case.

A comparison of experimental and calculated section topograms shows that they are in good agreement, which means that the diffraction problem is quite accurately described by Takagi–Taupen equations. The analysis of the images presented leads to some interesting conclusions.

Figure 27 shows the function of efficient disorientations calculated for the edge dislocation for (220) reflection. The form of the function of local disorientations shows that it has two symmetry planes, βx and βy. At the same time, the experimental and calculated images of the edge dislocation have only one symmetry plane xz. Of course, the βx plane is the inversion reflecting plane, but this cannot break the image symmetry. To understand why this occurs, it is necessary to recall some conclusions of geometrical optics.

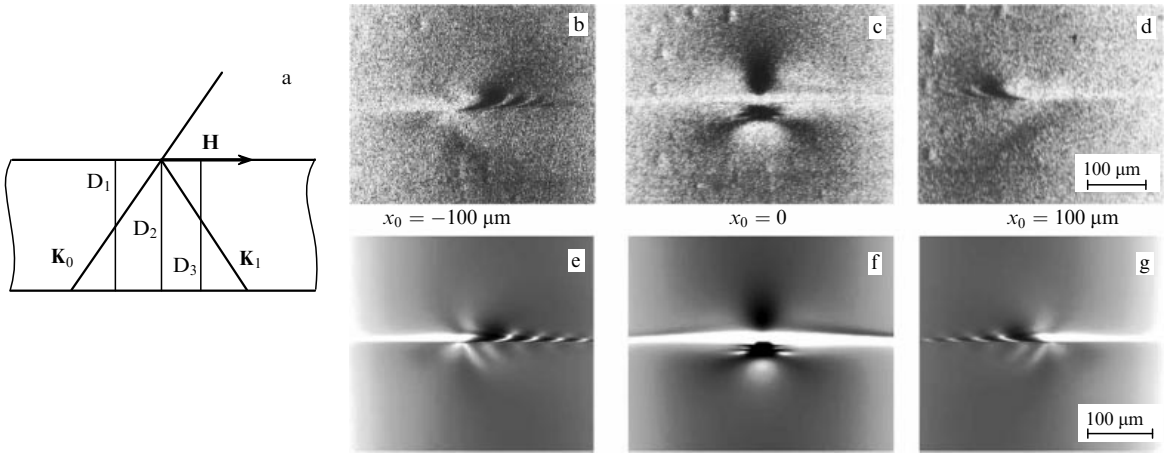

Figure 26. (a) X-ray schematic for obtaining section topograms. (b–d) Experimental section topograms obtained for three dislocation positions D_1, D_2, and D_3 in the scattering triangle. (e–g) Section topograms simulated with the help of Takagi equations and corresponding to experiments. x_0 is the dislocation position in the base of the scattering triangle. Si material, (220) reflection, and $CuK_{\alpha 1}$ radiation [102].

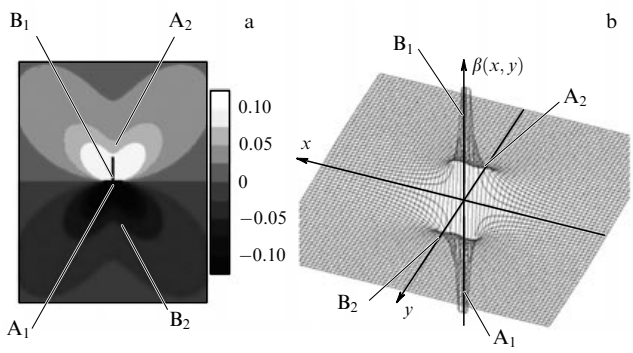

Figure 27. (Color online). Function $\beta(x, y)$ of local disorientations for (220) reflecting planes: (a) projection of the disorientation function on the xy plane, and (b) three-dimensional image of the function $\beta(x, y)$. Points A_1, A_2, B_1, B_2 denote regions with different signs of curvature of $\beta(x, y)$ [102].

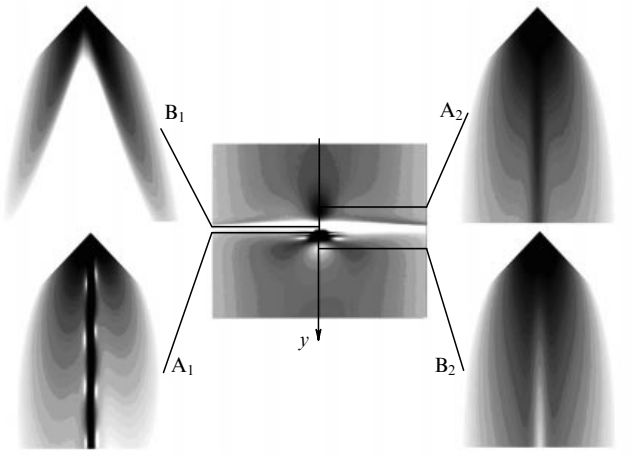

Figure 28. Numerical simulations of the section topogram with the image of the edge dislocation located in the middle of the scattering triangle along its bisector and four sections (A_1, A_2, B_1, B_2) of the wave field in the scattering triangle at different distances y from the dislocation axis: $y = 5$ μm (A_1), $y = 105$ μm (A_2), $y = -5$ μm (B_1), and $y = 105$ μm (B_2) [103].

Figure 28 presents computer-simulated wave-field distributions in the sections parallel to the scattering plane near a strongly distorted dislocation region. The sections are calculated for $y = \pm 5$ μm and $y = \pm 105.0$ m. In this case, the dislocation axis passes through the bisector of the scattering triangle with coordinates (0, 0). One can see that the surface of the function of local disorientations has regions with different signs of the function curvature. For example, in regions A_1 and A_2, the anomalous waves are focused, whereas the normal waves are defocused. Therefore, dark spots are observed in these regions. On the other hand, the normal waves are focused in regions B_1 and B_2, while the anomalous waves are defocused, and light spots are naturally observed in these regions. Thus, the reason for the discrepancy between the shape of the field of local disorientations and the dislocation image in section topography becomes clear.

Notice that the section dislocation images obtained do not yield the form of a rosette of effective angular disorientations. At the same time, dislocation images in the methods of scan topograms, anomalous X-ray propagation, and electron microscopy virtually correspond to the rosette of effective angular disorientations [70, 99–101]. The latter circumstance is explained, first of all, by the fact that each point of a defect is always imaged by a strip with the length determined by the crystal thickness and diffraction angle, and the fine details of the contrast observed in Fig. 28 are smoothed upon averaging.

6. Conclusions

Thus, each point of a strongly distorted region of an elastic field near a dislocation core can be treated as a source of a new wave field propagating under the dislocation in a new scattering triangle, similarly to scattering from the interface (the Borrmann–Lehmann effect) [61–64]. This 'new field' is coherent with the primary field, being produced by the latter due to interbranch scattering, and therefore interferes with the primary wave field to form the observed diffraction image of the dislocation.

The analysis of experimental section topograms and images obtained in computer simulations leads to the main conclusion that the structure of the dislocation image cardinally depends on its position in the scattering triangle. This is related to the structure of the wave field of transmitted and diffracted waves in the scattering triangle [40, 65].

A comparison of different dislocation orientations in the Borrmann triangle allows us to estimate the role of various effects determined by the interference of the initial wave field with a new wave field produced in the strongly distorted crystal region. Analysis of various phenomena described in this paper permits us to determine the dislocation parameters [56, 57] and to optimize the diffraction conditions of topographic survey for investigating characteristics of an elastic field.

A direct or kinematic dislocation image is presented in section topograms only when the strongly distorted region near the dislocation core intersects the incident beam. In this case, a bright projector appears in the region of intersection of the incident beam with the dislocation axis, which gives light in the direction of the diffracted beam. This is just the direct image of the dislocation. Its position in a section topogram allows one to determine quite accurately the level depth of the dislocation under the crystal surface. Notice that the direct image appears only when the disorientation value exceeds the diffraction reflecting region [91, 92].

As the dislocation axis moves away from the primary beam, the brightness of this projector noticeably decreases, the monolith beam splits into numerous interference rays, and a light shadow appears near it on the side of the primary beam, caused by the redistribution of the wave field within the scattering triangle. It is this contrast that A Authier called the dynamical image.

References

1. Berg W *Naturwissenschaften* **19** 391 (1931)
2. Berg W *Z. Kristallogr.* **89** 286 (1934)
3. Barrett C S *Trans. AIME* **161** 15 (1945)
4. Schulz L G *Trans. AIME* **200** 1082 (1954)
5. Fujiwara T *Memo. Defense Acad.* **2** (5) 127 (1963)
6. Fujiwara T, Dohi S, Takeda T *Memo. Defense Acad.* **3** (2) 17 (1963)
7. Turner A P, Vreeland T (Jnr.), Pope D P *Acta Cryst. A* **24** 452 (1968)
8. Bonse U *Z. Phys.* **153** 278 (1958)
9. Kohra K *J. Phys. Soc. Jpn.* **17** 589 (1962)
10. Kohra K, Kikuta S *Acta Cryst. A* **24** 200 (1968)
11. Lang A R *Acta Cryst.* **12** 249 (1959)
12. Authier A *Adv. X-Ray Analysis* **10** 9 (1967)
13. Darwin C G *Phil. Mag.* **27** 315 (1914)
14. Ewald P P *Ann. Physik* **49** 117 (1916)
15. v. Laue M *Ergebnexant Naturwiss.* **10** 133 (1931)
16. Cowley J M *Diffraction Physics* (Amsterdam: North-Holland, 1975; Translated into Russian *Fizika Difraktsii* (Moscow: Mir, 1979)
17. James R W *The Crystalline State* (Eds Sir W H Bragg, W L Bragg) Vol. 2 *The Optical Principles of the Diffraction of X-Rays* (London: G. Bell and Sons, 1948); Translated into Russian *Opticheskie printsypy difraktsii rentgenovskikh luchei* (Moscow: IL, 1950)
18. Takagi S *J. Phys. Soc. Jpn.* **13** 278 (1958)
19. Penning P, Polder D *Philos. Res. Rep.* **16** (4) 499 (1961)
20. Penning P, Polder D *Philos. Res. Rep.* **16** (5) 419 (1961)
21. Kato N *Acta Cryst.* **16** 276 (1963)
22. Kato N *Acta Cryst.* **16** 282 (1963)
23. Kato N *J. Phys. Soc. Jpn.* **18** 1785 (1963)
24. Kato N *J. Phys. Soc. Jpn.* **19** 67 (1964)
25. Kato N *J. Phys. Soc. Jpn.* **19** 971 (1964)
26. Patel J R, Kato N *Appl. Phys. Lett.* **13** 40 (1968)
27. Kato N, Patel J R *J. Appl. Phys.* **44** 965 (1973)
28. Patel J R, Kato N *J. Appl. Phys.* **44** 971 (1973)
29. Ando Y, Patel J R, Kato N *J. Appl. Phys.* **44** 4405 (1973)
30. Dederichs P H *Phys. Status Solidi B* **23** 377 (1967)
31. Dederichs P H *Phys. Rev. B* **1** 1306 (1970)
32. Krivoglaz M A *Theory of X-ray and Thermal-Neutron Scattering by Real Crystals* (New York: Plenum Press, 1969); Translated from Russian: *Teoriya Rasseyaniya Rentgenovskikh Luchei i Teplovykh Neitronov Real'nymi Kristallami* (Moscow: Nauka, 1967)
33. Krivoglaz M A *X-ray and Neutron Diffraction in Nonideal Crystals* (Berlin: Springer, 1996); Translated from Russian: *Difraktsiya Rentgenovskikh Luchei i Neitronov v Neideal'nykh Kristallakh* (Kiev: Naukova Dumka, 1983)
34. Takagi S *Acta Cryst.* **15** 1311 (1962)
35. Takagi S *J. Phys. Soc. Jpn.* **27** 1239 (1969)
36. Taupen D *Bull. Soc. Franc. Mineral. Cryst.* **87** 469 (1964)
37. Taupen D *Acta Cryst.* **23** 25 (1967)
38. Tanner B K, Phil M A *X-Ray Diffraction Topography* (New York: Pergamon Press, 1966)
39. Bowen D K, Tanner B K *High Resolution X-Ray Diffractometry and Topography* (New York: Taylor and Francis, 1998); Translated into Russian: *Vysokorazreshayushchaya Rentgenovskaya Difraktometriya i Topografiya* (St. Petersburg: Nauka, 2002)
40. Authier A *Dynamical Theory of X-Ray Diffraction* (Oxford: Science Publ., 2001)
41. Elistratov A M, in *Pryamye Metody Issledovaniya Defektov v Kristallakh* (Direct Methods for Studying Defects in Crystals) (Ed. A M Elistratov) (Moscow: Mir, 1965) p. 268
42. Hirsh P B et al. *Electron Microscopy of Thin Crystals* (London: Butterworths, 1965); Translated into Russian: *Elektronnaya Mikroskopiya Tonkikh Kristallov* (Moscow: Mir, 1968)
43. Indenbom V L, Chukhovskii F N *Sov. Phys. Usp.* **15** 298 (1972); *Usp. Fiz. Nauk* **107** 229 (1972)
44. Indenbom V L, Chukhovskii F N *Sov. Phys. Crystallogr.* **16** 972 (1971); *Kristallografiya* **16** 1101 (1971)
45. Kohn V G *Crystallogr. Rep.* **52** 598 (2007); *Kristallografiya* **52** 625 (2007)
46. Amelinckx S *The Direct Observation of Dislocations* (New York: Academic Press, 1964); Translated into Russian: *Metody Pryamogo Nablyudeniya Dislokatsii* (Moscow: Mir, 1968)
47. Borrmann G *Z. Phys.* **42** 157 (1941)
48. Borrmann G *Z. Phys.* **127** 297 (1950)
49. Iveronova V I, Revkevich G P *Teoriya Rasseyaniya Rentgenovskikh Luchei* (Theory of X-Ray Scattering) (Moscow: Izd. MGU, 1978)
50. Pinsker Z G *Dynamical Scattering of X-Rays in Crystals* (New York: Springer, 1978); Translated from Russian: *Rentgenovskaya Kristallooptika* (X-Ray Crystal Optics) (Moscow: Nauka, 1982)
51. Suvorov É V, Smirnova I A *Phys. Solid State* **52** 258 (2010); *Fiz. Tverd. Tela* **52** 241 (2010)
52. Shul'pina I L, Petrashen' P V, Osmakova O Yu, in *Dinamicheskie Effekty Rasseyaniya Rentgenovskikh Luchei i Elektronov, 4-e Soveshchanie, Leningrad, 31 Marta–2 Aprelya* (Dynamic Aspects of X-Ray and Electron Scattering, Fourth Meeting, Leningrad, 31 March–2 April 1976, Theses of Papers) (Leningrad: LIYaF, 1976) p. 50
53. Petrashen P V, Shulpina I L *Phys. Status Solidi A* **78** K105 (1983)
54. Danil'chuk L N, Nikitenko V I *Fiz. Tverd. Tela* **9** 2027 (1967)
55. Suvorov E V et al. *Phys. Status Solidi A* **26** 385 (1974)
56. Indenbom V L, Nikitenko V I, Suvorov E V, Kaganer V M *Phys. Status Solidi A* **46** 379 (1978)
57. Suvorov E V et al. *Phys. Status Solidi A* **54** 29 (1979)
58. Kato N *Acta Cryst.* **14** 526 (1961)
59. Aristov V V et al. *Phys. Status Solidi A* **72** 483 (1982)
60. Suvorov E V, Polovinkina V I, Nikitenko V I *Sov. Phys. Solid State* **13** 2253 (1972); *Fiz. Tverd. Tela* **13** 2692 (1971)
61. Borrmann G, Lehmann K *Crystallography and Crystal Perfection* (Ed. G N Ramachandran) (London: Academic Press, 1963) p. 101
62. Lehmann K, Borrmann G *Z. Kristallogr.* **125** 234 (1967)
63. Shulakov E V, Smirnova I A, Suvorov E V *Poverkhnost'. Rentgen. Sinkhrotron. Neitron. Issled.* (7) 32 (1996)
64. Shulakov E V, Smirnova I A, Suvorov E V *Poverkhnost'. Rentgen. Sinkhrotron. Neitron. Issled.* (1) 101 (2002)
65. Indenbom V L, Slobodetskii I Sh, Truni K G *Sov. Phys. JETP* **39** 542 (1974); *Zh. Eksp. Teor. Fiz.* **66** 1110 (1974)
66. Suvorov É V, Polovinkina V I *JETP Lett.* **20** 145 (1974); *Pis'ma Zh. Eksp. Teor. Fiz.* **20** 326 (1974)
67. Indenbom V L, Chukhovskii F N *Kristallografiya* **19** 35 (1974)
68. Indenbom V L, Slobodetskii I Sh *Kristallografiya* **19** 42 (1974)
69. Suvorov E V, Mukhin K Yu, in *Dinamicheskie Effekty Rasseyaniya Rentgenovskikh Luchei i Elektronov, 4-e Soveshchanie, Leningrad, 31 Marta–2 Aprelya* (Dynamic Aspects of X-Ray and Electron

Scattering, Fourth Meeting, Leningrad, 31 March–2 April 1976, Abstracts of Papers) (Leningrad: LIYaF, 1976) p. 42
70. Hirth J P, Lothe J *Theory of Dislocations* (New York: McGraw-Hill, 1968); Translated into Russian: *Teoriya Dislokatsii* (Moscow: Atomizdat, 1972)
71. de Wit R *Phys. Status Solidi B* **20** 567 (1967)
72. Brümmer O, Stephanik H *Dynamische Interferenztheorie. Grundlagen und Anwendungen bei Röntgenstrahlung, Elektronen und Neutronen* (Leipzig: Akademische Verlagsgesellschaft Geest und Portig K.-G., 1976)
73. Epelboin Y, Riglet P *Phys. Status Solidi A* **54** 547 (1979)
74. Chukhovskii F N, Shtolberg A A *Phys. Status Solidi B* **41** 815 (1970)
75. Authier A *Bull. Soc. Franc. Mineral. Cristallogr.* **84** 51 (1961)
76. Balibar F, Authier A *Phys. Status Solidi B* **21** 413 (1967)
77. Indenbom V L, Nikitenko V I, Suvorov E V, Kaganer V M *Phys. Status Solidi A* **46** 379 (1978)
78. Suvorov E V et al. *Phys. Status Solidi A* **60** 27 (1980)
79. Indenbom V L, Kaganer V M, Möhling W, Suvorov E V *Phys. Status Solidi A* **83** 195 (1984)
80. Suvorov E V, Smirnova I A, Shulakov E V *Poverkhnost'. Rentgen. Sinkhrotron. Neitron. Issled.* (4) 100 (2004)
81. Shulpina I L, Datsenko L I *Ukr. Fiz. Zh.* **12** 1474 (1967)
82. Erofeev V N, Nikitenko V I, Polovinkina V I, Suvorov E V *Sov. Phys. Crystallogr.* **16** 151 (1971); *Kristallografiya* **16** 190 (1971)
83. Suvorov E V, Shulpina I L *Poverkhnost'. Rentgen. Sinkhrotron. Neitron. Issled.* (7) 3 (2001)
84. Shulpina I L, Suvorov E V *Bull. Russ. Acad. Sci. Phys.* **74** 1488 (2010); *Izv. Ross. Akad. Nauk Ser. Fiz.* **74** 1547 (2010)
85. Suvorov E V, Smirnova I A *Phys. Solid State* **52** 2485 (2010); *Fiz. Tverd. Tela* **52** 2325 (2010)
86. Indenbom V L, Kaganer V M, Suvorov E V *Sov. Phys. JETP* **59** 394 (1984); *Zh. Eksp. Teor. Fiz.* **86** 675 (1984)
87. Smirnova I A, Suvorov E V, Shulakov E V *Poverkhnost'. Rentgen. Sinkhrotron. Neitron. Issled.* (12) 1 (2006)
88. Suvorov E V, Smirnova I A, Shulakov E V *Poverkhnost'. Rentgen. Sinkhrotron. Neitron. Issled.* (9) 1 (2007)
89. Suvorov E V, Smirnova I A *Poverkhnost'. Rentgen. Sinkhrotron. Neitron. Issled.* (12) 1 (2011)
90. Suvorov E V, Smirnova I A *Tech. Phys. Lett.* **38** 991 (2012); *Pis'ma Zh. Tekh. Fiz.* **38** (21) 70 (2012)
91. Kyutt R N, Ruvimov S S, Shulpina I L *Tech. Phys. Lett.* **32** 1079 (2006); *Pis'ma Zh. Tekh. Fiz.* **32** (24) 79 (2006)
92. Mil'vidskii M G et al. *Poverkhnost'. Rentgen. Sinkhrotron. Neitron. Issled.* (4) 5 (2001)
93. Suvorov E V, Smirnova I A, Shulakov E V *Poverkhnost'. Rentgen. Sinkhrotron. Neitron. Issled.* (11) 74 (2004)
94. Suvorov E V, Smirnova I A, Shulakov E V *Poverkhnost'. Rentgen. Sinkhrotron. Neitron. Issled.* (12) 12 (2005)
95. Suvorov E V, Smirnova I A, Shulakov E V, Alezhko-Ozhevskii O P *Poverkhnost'. Rentgen. Sinkhrotron. Neitron. Issled.* (1) 99 (2000)
96. Bonse U, Hart M *Appl. Phys. Lett.* **6** 155 (1965)
97. Bonse U, Hart M *Appl. Phys. Lett.* **7** 99 (1965)
98. Hart M *Proc. R. Soc. London A 3***09** 281 (1969)
99. Danil'chuk L N, Smorodina T A *Fiz. Tverd. Tela* **7** 1245 (1965)
100. Danil'chuk L N, Georgiev A I *Kristallografiya* **11** 2349 (1966)
101. Danil'chuk L N, Nikitenko V I *Fiz. Tverd. Tela* **9** 2027 (1967)
102. Smirnova I A, Suvorov É V, Shulakov E V *Phys. Solid State* **49** 1104 (2007); *Fiz. Tverd. Tela* **49** 1050 (2007)
103. Suvorov E V, Smirnova I A *Poverkhnost'. Rentgen. Sinkhrotron. Neitron. Issled.* (10) 7 (2008)